













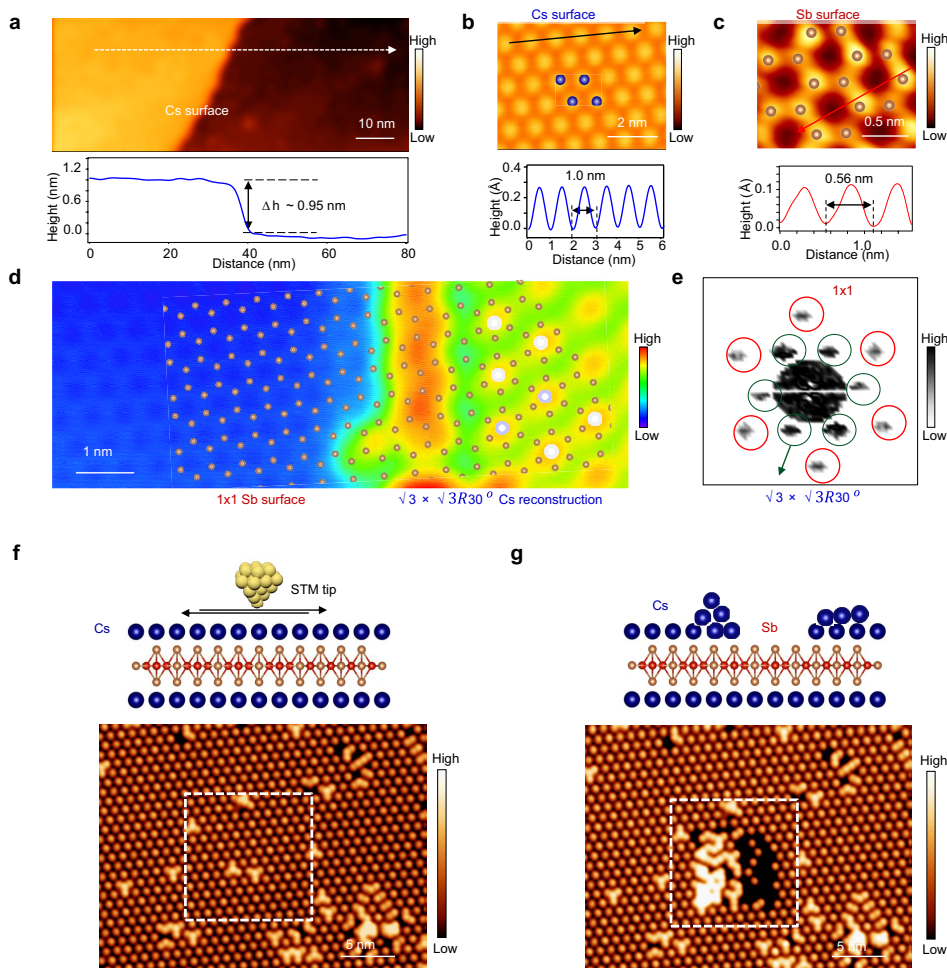
31. Berg, E., Fradkin, E. & Kivelson, S. A. Charge-4e superconductivity from pair-density-wave order in certain high-temperature superconductors. *Nat. Phys.* **5**, 830–833 (2009).
32. Lee, P. A. Amperean pairing and the pseudogap phase of cuprate superconductors. *Phys. Rev. X* **4**, 031017 (2014).
33. Agterberg, D. F. et al. The physics of pair-density waves: cuprate superconductors and beyond. *Annu. Rev. Condens. Matter Phys.* **11**, 231–270 (2020).
34. Liu, X., Chong, Y. X., Sharma, R. & Davis, J. C. S. Discovery of a Cooper-pair density wave state in a transition-metal dichalcogenide. *Science* **372**, 1447–1452 (2021).
35. Landau, L. On the theory of superfluidity. *Phys. Rev.* **75**, 884–885 (1949).
36. Feynman, R. P. in *Progress in Low Temperature Physics* Vol. 1 (ed. Gorter, C. J.) 17–53 (Elsevier, 1955).
37. Feynman, R. P. & Cohen, M. Energy spectrum of the excitations in liquid helium. *Phys. Rev.* **102**, 1189–1204 (1956).
38. Nozières, P. Is the roton in superfluid  $^4\text{He}$  the ghost of a Bragg spot? *J. Low Temp. Phys.* **137**, 45–67 (2004).
39. Edkins, S. D. et al. Magnetic field-induced pair density wave state in the cuprate vortex halo. *Science* **364**, 976–980 (2019).
40. Dai, Z., Zhang, Y.-H., Senthil, T. & Lee, P. A. Pair-density waves, charge-density waves, and vortices in high- $T_c$  cuprates. *Phys. Rev. B* **97**, 174511 (2018).
41. Yu, S. L. & Li, J. X. Chiral superconducting phase and chiral spin-density-wave phase in a Hubbard model on the kagome lattice. *Phys. Rev. B* **85**, 144402 (2012).
42. Kiesel, M. L., Platt, C. & Thomale, R. Unconventional Fermi surface instabilities in the kagome Hubbard model. *Phys. Rev. Lett.* **110**, 126405 (2013).
43. Wang, W. S., Li, Z. Z., Xiang, Y. Y. & Wang, Q. H. Competing electronic orders on kagome lattices at van Hove filling. *Phys. Rev. B* **87**, 115135 (2013).

**Publisher's note** Springer Nature remains neutral with regard to jurisdictional claims in published maps and institutional affiliations.

© The Author(s), under exclusive licence to Springer Nature Limited 2021

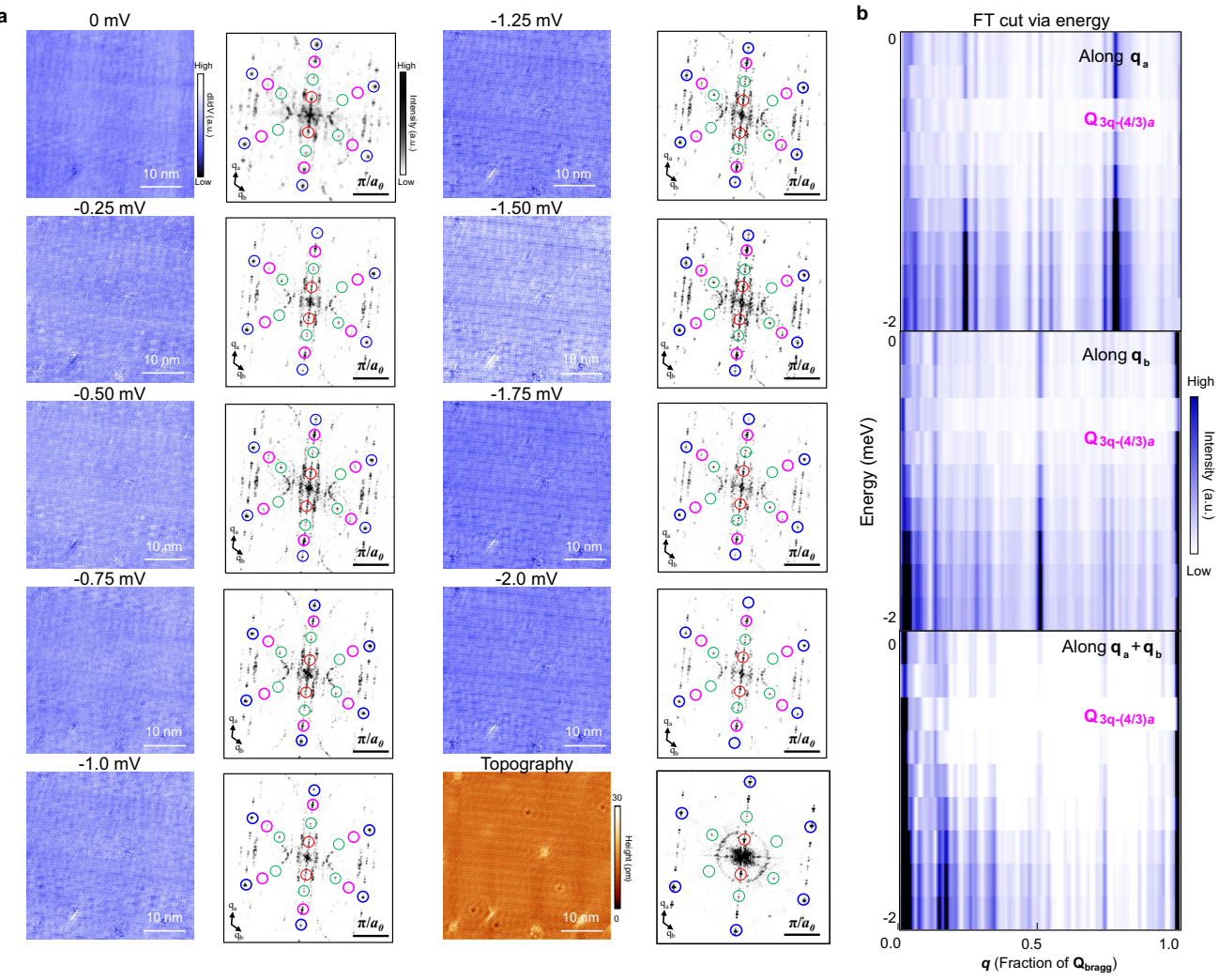






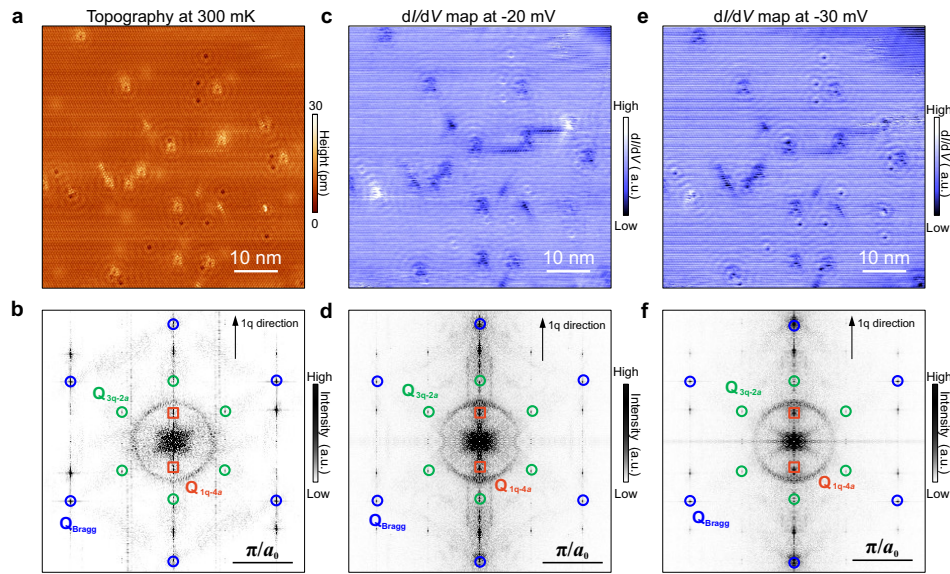
**Extended Data Fig. 1 | Detailed STM characterization of the Sb and Cs surfaces.** **a**, Top panel: a typical STM image showing a step edge of Cs surface. Bottom panel: line profile along the white dotted arrow in **a**, indicating that the height of the step edge is  $\sim 0.95$  nm, which is consistent with the calculated interlayer distance ( $V_s = -1$  V,  $I_t = 0.1$  nA). **b**, Atomically-resolved STM image of Cs surface, showing a hexagonal lattice with a period of 1.0 nm, which is  $\sqrt{3}$  times larger than the lattice constant ( $a = b = 0.55$  nm, see Fig. S1a). ( $V_s = -500$  mV,  $I_t = 0.5$  nA). **c**, Atomically-resolved STM image of Sb surface, showing a honeycomb lattice. The periodicity of the honeycomb lattice is about 0.56 nm, which agrees with the bulk lattice constant ( $a = b = 0.55$  nm, see Fig. S1a).

( $V_s = -500$  mV,  $I_t = 0.5$  nA). **d**, Atomically-resolved STM image of an interface between the top Cs and bottom Sb surfaces (same as in Fig. 1d). The atomic model is overlaid on the image, showing that each Cs atom sits on top of the Sb honeycomb center ( $V_s = -500$  mV,  $I_t = 0.5$  nA). **e**, FFT of **d** showing the Cs  $\sqrt{3} \times \sqrt{3}R30^\circ$  reconstruction relative to the Sb  $1 \times 1$  lattice. **f**, **g**, Top panels: schematics showing STM manipulations to expose the bottom Sb surface. Bottom panels: STM images of Cs surface before (**f**) and after (**g**) STM manipulation, respectively, showing the freshly-obtained bottom Sb surface highlighted by the white dotted square ( $V_s = -500$  mV,  $I_t = 0.5$  nA).



**Extended Data Fig. 2 | STM topography and  $dI/dV$  maps over a  $40 \text{ nm} \times 40 \text{ nm}$  region at 300 mK.** **a**, Topography,  $dI/dV$  maps and the intensity of the drift-corrected Fourier transforms at the sample bias from -2 mV to 0 mV,

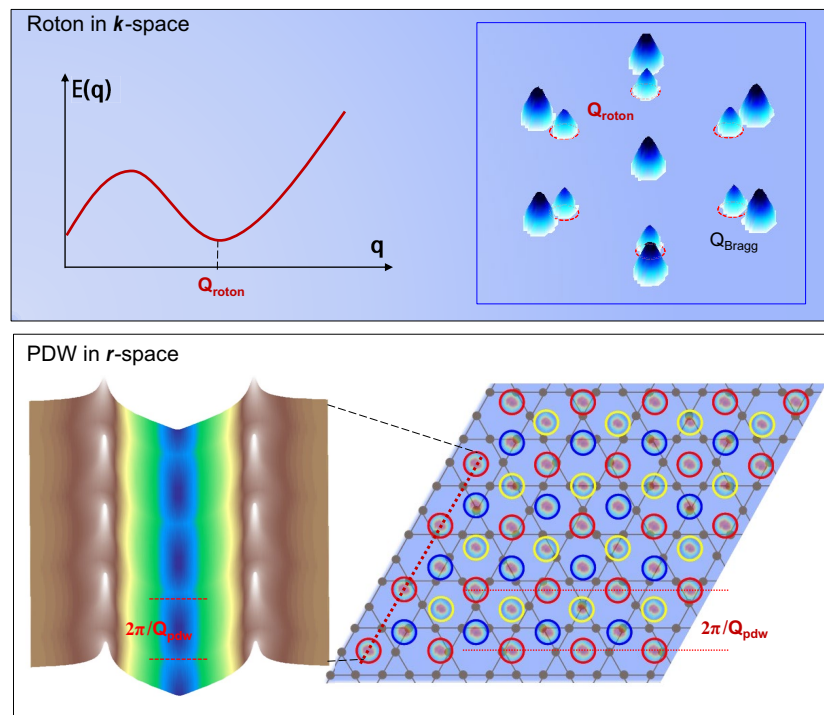
respectively. Each map consists of 500 pixels  $\times$  500 pixels. **b**, Energy dependence of the Fourier line cuts along the three directions of the hexagonal zone. ( $V_s = -5 \text{ mV}$ ,  $I_t = 2 \text{ nA}$ ,  $V_{\text{mod}} = 0.5 \text{ mV}$ ).



**Extended Data Fig. 3 | Absence of  $4a_0/3$  in high energy  $dI/dV$  maps at 300 mK.**

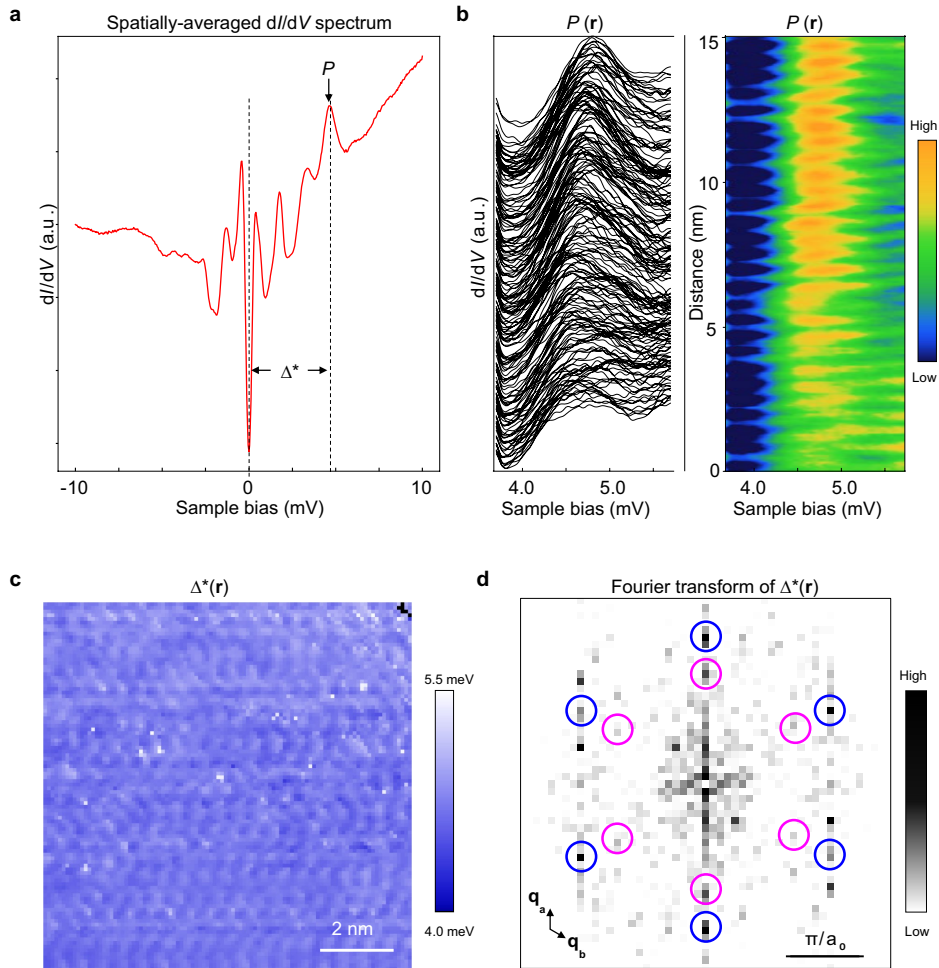
**a**, Large-scale STM image ( $60 \text{ nm} \times 60 \text{ nm}$ ) of the Sb surface obtained at the temperature below  $T_c$  (300 mK), where a unidirectional charge order is visible ( $V_s = -20 \text{ mV}, I_t = 2 \text{nA}$ ). **b**, The magnitude of drift-corrected Fourier transform of **a**, showing clearly the  $\mathbf{Q}_{3q-2a}$  CDW and  $\mathbf{Q}_{1q-4a}$  stripe CDW peaks. **c, d**,  $dI/dV$  mapping

( $1024 \text{ pixels} \times 1024 \text{ pixels}$ ) over the same region at -20 mV and the corresponding magnitude of drift-corrected Fourier transform ( $V_s = -20 \text{ mV}, I_t = 2 \text{nA}, V_{mod} = 0.2 \text{ mV}$ ). **d, f**,  $dI/dV$  mapping ( $1024 \text{ pixels} \times 1024 \text{ pixels}$ ) over the same region at -30 mV and the corresponding magnitude of drift-corrected Fourier transform ( $V_s = -30 \text{ mV}, I_t = 2 \text{nA}, V_{mod} = 0.2 \text{ mV}$ ).



**Extended Data Fig. 4 | Schematic illustration of the roton-PDW.** Top panel: the roton dispersion and roton minimum at  $\mathbf{Q}_{\text{roton}} = \mathbf{Q}_{3q-4a/3}$  in the reciprocal lattice. Bottom panel: the 3Q roton-PDW at  $\mathbf{Q}_{\text{pdw}} = \mathbf{Q}_{\text{roton}}$  forming a

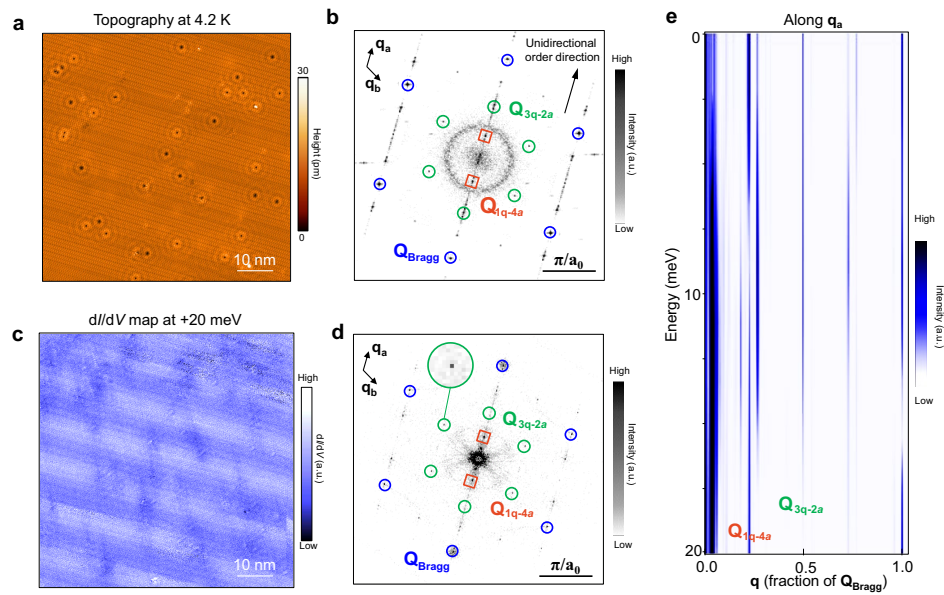
commensurate vortex-antivortex lattice (red, blue and yellow circles) that spatially modulates the tunneling conductance spectra along a line cut.



**Extended Data Fig. 5 | Spatial map of pseudogap and  $Q_{3q-4a_3}$  modulations.**

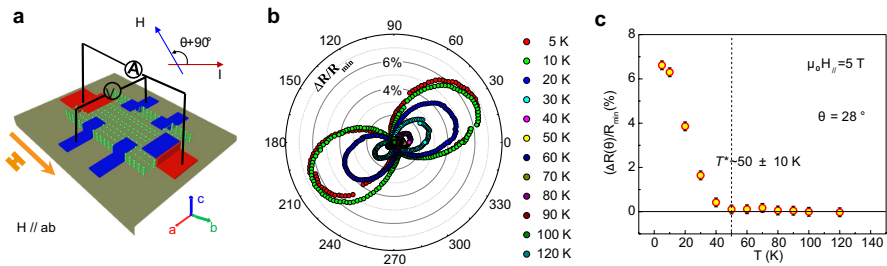
**a**, Spatially-averaged  $dI/dV$  spectrum obtained below  $T_c$ , exhibiting several peaks in the energy range between 1 mV and 6 mV ( $V_s = -10$  mV,  $I_t = 1$  nA,  $V_{mod} = 0.05$  mV). The PDW pseudogap peak located near 5 mV is labelled as  $P$ . **b**, Waterfall and color plot of a  $dI/dV$  line cut, showing spatial modulations of

the peak  $P$  ( $V_s = -3.7$  mV,  $I_t = 1$  nA,  $V_{mod} = 0.05$  mV). **c**, Spatial gap map of  $\Delta^*(r)$ , showing the spatial modulations of the pseudogap ( $V_s = -3.7$  mV,  $I_t = 1$  nA,  $V_{mod} = 0.05$  mV). **d**, Fourier transform of the pseudogap map showing peaks at the PDW vectors  $Q_{3q-4a_3}$  circled in magenta.



**Extended Data Fig. 6 | Charge ordered normal state in  $\text{CsV}_3\text{Sb}_5$  above  $T_c$ .**  
**a,b** Large-scale STM topography of Sb surface obtained at 4.2 K and the magnitude of drift-corrected Fourier transform, showing  $2a_0 \times 2a_0$  and  $4a_0$  striped CDW peaks at wave vectors  $\mathbf{Q}_{3q-2a}$  and  $\mathbf{Q}_{1q-4a}$  ( $V_s = -90$  mV,  $I_t = 2$  nA).

**c,d**  $dI/dV$  mapping of **a** at 20 mV and the magnitude of drift-corrected Fourier transform, respectively ( $V_s = -90$  mV,  $I_t = 2$  nA,  $V_{mod} = 0.5$  mV). **e**. Energy dependence of the Fourier line cuts along  $\mathbf{q}_a$  directions, showing that peaks at  $\mathbf{Q}_{3q-2a}$  and  $\mathbf{Q}_{1q-4a}$  at 4 K are non-dispersive ( $V_s = -90$  mV,  $I_t = 2$  nA,  $V_{mod} = 0.5$  mV).



**Extended Data Fig. 7 | Normal state angular-dependent magnetoresistance.**

**a**, Schematic of the in-plane resistance measurement under a 5 T magnetic field by rotating the sample along c axis of the single crystal. **b**, Angular plot of the normalized anisotropic magnetoresistance ( $\Delta R / R_{min}$ ,  $\Delta R = R(\theta) - R_{min}$ ), showing

two-fold symmetry at the temperature below  $\sim 50$  K.  $\theta$  is defined in **a**.

**c**, Temperature dependence of the angular-dependent of at  $\Delta R / R_{min}$  the angle of  $28^\circ$ , showing the onset of two-fold rotational symmetry below  $T^* \sim 50 \pm 10$  K.